

pubs.acs.org/NanoLett Letter

Synthesis and Polymorph Manipulation of FeSe₂ Monolayers

Zehao He, [∇] Shiva Prasad Poudel, [∇] Samuel Stolz, [∇] Tianye Wang, Antonio Rossi, Feng Wang, Sung-Kwan Mo, Alexander Weber-Bargioni, Zi Qiang Qiu, Salvador Barraza-Lopez, Tiancong Zhu,* and Michael F. Crommie*



Cite This: Nano Lett. 2024, 24, 8535-8541



ACCESS

III Metrics & More

Article Recommendations

s Supporting Information

ABSTRACT: Polymorph engineering involves the manipulation of material properties through controlled structural modification and is a candidate technique for creating unique two-dimensional transition metal dichalcogenide (TMDC) nanodevices. Despite its promise, polymorph engineering of magnetic TMDC monolayers has not yet been demonstrated. Here we grow FeSe₂ monolayers via molecular beam epitaxy and find that they have great promise for magnetic polymorph engineering. Using scanning tunneling microscopy (STM) and spectroscopy (STS), we find that FeSe₂ monolayers predominantly display a 1T' structural polymorph at 5 K. Application of voltage pulses from an STM tip causes a local, reversible transition from the 1T' phase to the 1T phase. Density

Polymorph engineering of FeSe₂ monolayers

1T' polymorph
electrical switching
thermal switching

0.5 nm

functional theory calculations suggest that this single-layer structural phase transition is accompanied by a magnetic transition from an antiferromagnetic to a ferromagnetic configuration. These results open new possibilities for creating functional magnetic devices with TMDC monolayers via polymorph engineering.

KEYWORDS: polymorphism, magnetism, two-dimensional materials, scanning tunneling microscopy, phase transitions, density functional theory

MDC monolayers have demonstrated great potential for next-generation electronic, magnetic, and optical applications. These atomically thin materials host a variety of novel phenomena, including nontrivial topology,^{2–4} superconductivity,^{5,6} charge density waves,^{5,7–9} magnetism,^{10,11} and Mott insulating phases,^{6,12,13} most of which can be strongly tuned through electrostatic gating and strain. 14-18 The coexistence of different crystal structures having the same stoichiometries in TMDC monolayers provides unique opportunities for TMDC polymorph engineering. The three main polymorphs for TMDC monolayers are the trigonal prismatic (1H), octahedral (1T), and distorted octahedral (1T') lattices, each of which exhibits very different physical properties. Structural manipulation between TMDC monolayer polymorphs has been used to induce topological transitions between the 1T' and 1H phases in WSe₂ and MoTe₂, ^{19,20} as well as metal–insulator transitions between the 1H and 1T phases of TaSe2, TaS2, and NbSe₂. ^{21–23} Polymorph engineering of TMDC monolayers has been achieved through temperature, 24 strain, 14 charge doping, ^{15,16} laser irradiation, ²⁵ and application of local electric fields, ^{21–23,26} thus expanding the toolbox for creating functional devices based on TMDC monolayers. Despite rapid progress in experimentally controlling polymorphism in TMDC monolayers, however, the manipulation of magnetism in these materials through polymorph engineering is still in its infancy, mainly due to a lack of suitable material platforms.

Here we demonstrate that monolayer FeSe₂ is a promising candidate for magnetic polymorph engineering through a combined experimental and theoretical investigation. The FeSe₂ monolayers used in this study were grown via molecular beam epitaxy (MBE). Scanning tunneling microscopy (STM) investigation reveals that our FeSe2 monolayers occur mainly in a stripe phase that we identify as the 1T' polymorph. We find that FeSe2 monolayers can be locally converted into a hexagonal phase that we identify as the 1T-FeSe2 polymorph upon the application of voltage pulses from the STM tip. This phase transition can be reversed by heating the sample above 50 K, thus establishing the 1T' polymorph as the ground state structure. DFT+U calculations confirm the assignment of 1T' and 1T polymorphs to the stripe and hexagonal phases, respectively, and corroborate that 1T'-FeSe2 is the most stable polymorph and that it has a low energy barrier for structural phase transitions. Our calculations further suggest the existence of antiferromagnetic order in monolayer 1T'-FeSe2 and

Received: March 18, 2024 Revised: June 11, 2024 Accepted: June 12, 2024 Published: July 5, 2024





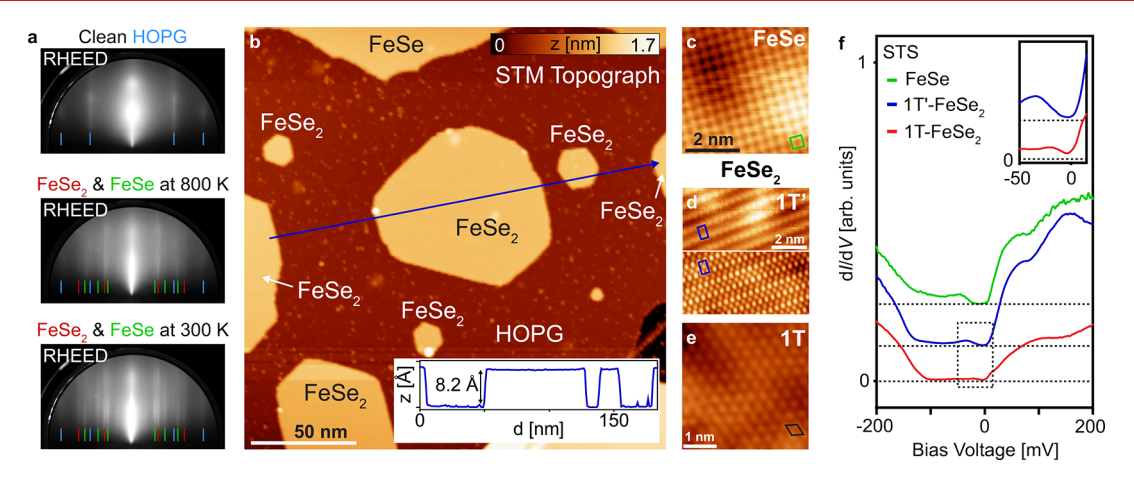


Figure 1. Growth and structural characterization of FeSe $_2$ monolayers. (a) RHEED patterns (top to bottom) of clean HOPG (blue), a mixture of monolayer FeSe $_2$ (red), and monolayer FeSe (green) after growth at 800 K and after cooling to 300 K. (b) Large-scale STM image of a typical MBE-grown sample ($V_B = -1.0 \text{ V}$; $I_T = 10 \text{ pA}$). The inset shows the height profile along the blue line. (c) Close-up STM image of an FeSe monolayer with a square unit cell (green) ($V_B = -1.0 \text{ V}$; $I_T = 100 \text{ pA}$). (d) Close-up STM image of monolayer 1T'-FeSe $_2$ with a rectangular unit cell (blue) (for the top panel, $V_B = -1.0 \text{ V}$ and $I_T = 10 \text{ pA}$; for the bottom panel, $V_B = -1.0 \text{ V}$ and $I_T = 100 \text{ pA}$). (e) Close-up STM image of the 1T-FeSe $_2$ monolayer with a hexagonal unit cell (black) ($V_B = -0.3 \text{ V}$; $I_T = 100 \text{ pA}$). (f) STS spectra of monolayer FeSe (green), 1T'-FeSe $_2$ (blue), and 1T-FeSe $_2$ (red) (lock-in $V_{mod} = 2 \text{ mV}$). The curves have been shifted vertically for easier viewing (dashed lines show dI/dV = 0 for each curve). The inset shows STS spectra in the low-bias range for monolayer 1T'-FeSe $_2$ (blue) and 1T-FeSe $_2$ (red) (lock-in $V_{mod} = 2 \text{ mV}$). Tip stabilization set point for STS: $V_B = -0.2 \text{ V}$, and $I_T = 100 \text{ pA}$.

ferromagnetic order in the monolayer 1T-FeSe_2 phase over a large range of values for the parameter U.

FeSe₂ monolayers were grown on highly oriented pyrolytic graphite (HOPG) using MBE under a Se-rich environment (see Methods for the details of growth). The growth was monitored using reflection high-energy electron diffraction (RHEED) as shown in Figure 1a. We observed the concurrent growth of FeSe and FeSe₂ monolayers. During growth at 800 K, the RHEED intensity from the FeSe₂ monolayer (red lines in Figure 1a) is stronger than the monolayer FeSe intensity (green lines in Figure 1a). When the temperature decreases to 300 K, the relative RHEED intensity of monolayer FeSe increases, indicating that monolayer FeSe₂ is a metastable phase.

Low-temperature (5 K) STM and scanning tunneling spectroscopy (STS) measurements were performed to gain insight into the structural and electronic properties of monolayer FeSe2. The large-scale STM image shown in Figure 1b depicts monolayer FeSe₂ islands on HOPG that have a step height of $\sim 8.2 \pm 0.2$ Å. The high-resolution STM images and STS data shown in Figure 1c-f enable us to differentiate the structure and density of states of monolayer FeSe versus monolayer FeSe₂. Monolayer FeSe (Figure 1c) is observed to have a square unit cell with a lattice constant of 3.8 \pm 0.1 Å, as seen previously.²⁷ Our STS spectra obtained from monolayer FeSe (Figure 1f, green curve) are also in agreement with previous STS measurements.²⁷ All non-FeSe monolayer islands are identified as FeSe2 and are observed to have two different polymorphs. A majority of the FeSe₂ monolayer islands show a stripe phase (Figure 1d), accounting for >90% of the total FeSe₂ island area. An atomically resolved image of the stripe phase reveals a rectangular unit cell with lattice constants of 3.9 \pm 0.1 and 6.7 \pm 0.1 Å (Figure 1d, bottom panel). The atomic structure and symmetry of the stripe phase are similar to previous observations of 1T'-WTe₂⁴ [although a slight period doubling in the long direction can be seen for FeSe2 (see Figure S1)]. The remaining fraction of the FeSe₂ monolayer islands exhibits a hexagonal phase with a lattice constant of 3.8

 \pm 0.1 Å (Figure 1e) that is consistent with the 1T or 1H TMDC polymorphs. STS measurements shown in the inset of Figure 1f reveal that both phases of monolayer FeSe₂ exhibit a nonvanishing dI/dV signal near the Fermi level, thus indicating metallic behavior.

Figure 2 shows the process by which the stripe phase of monolayer FeSe₂ can be locally converted into the hexagonal phase by applying a voltage pulse from the STM tip. Figure 2a shows an FeSe₂ island before tip pulsing, where most of the island is in the stripe phase (see the dashed line phase boundary). To induce a local phase change, the STM tip was positioned at the location indicated by the white cross in Figure 2b and a voltage pulse of 3.4 V was applied for 100 ms with the STM feedback loop open (for the tunnel set point, $V_{\rm B}$ = -1 V and $I_T = 10$ pA). After the pulse, the region near the tip pulse position is seen to convert from the stripe phase to the hexagonal phase (see the lower dashed line which indicates the created phase boundary). The close-up image in the inset of Figure 2b shows the hexagonal symmetry of the converted region (this region has an area similar to the altered regions observed in other STM-driven phase transitions^{21,28,29}). The rest of the island was converted from the stripe phase to the hexagonal phase by scanning the entire island with a bias voltage (V_B) of 3.5 V $(I_T = 10 \text{ pA})$ (Figure 2c). Once converted to the hexagonal phase, the island could not be changed back to the stripe phase by pulsing despite the application of numerous voltage pulses (V_{pulse}) in the range from -5 to 5 V.

To better characterize the phase conversion process, we systematically determined the threshold pulse voltage required to convert different stripe phase islands to the hexagonal phase. For each island, a low voltage pulse of 2 V was first applied (using the initial tunnel set point $V_{\rm B} = -1$ V and $I_{\rm T} = 10$ pA), and then incrementally higher pulses were applied up to a maximum of 5 V (using the same initial set point) until a tip-induced structural phase transition occurred. A histogram of the minimum voltage pulse required to cause local phase conversion at 5 K for different monolayer islands is plotted in

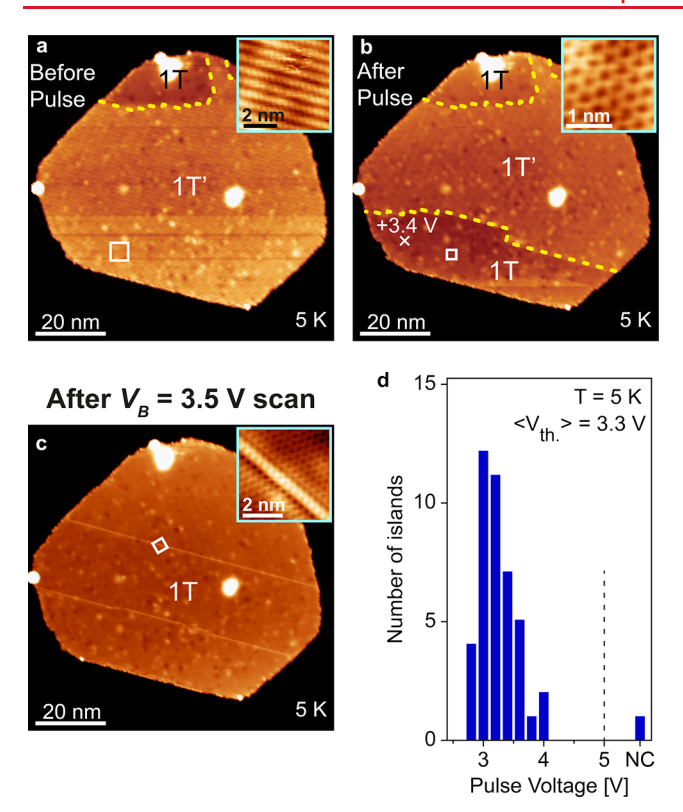


Figure 2. Electrically induced structural phase transition in FeSe₂ monolayers. (a) STM image of the stripe phase FeSe₂ monolayer island before any STM tip manipulation ($V_B = -1.0 \text{ V}$; $I_T = 10 \text{ pA}$). The boundary between the 1T' stripe phase and the 1T hexagonal phase of the FeSe₂ monolayer is indicated by a yellow dashed line. The inset shows a close-up image of the stripe phase ($V_B = -1.0 \text{ V}$; I_T = 10 pA). (b) Same island shown in panel (a) after a 3.4 V voltage pulse applied at the position indicated by the white x. The inset shows a close-up image of the hexagonal 1T phase ($V_{\rm B} = -1.0 \text{ V}$; $I_{\rm T} = 10$ pA). (c) Same island after STM scanning with $V_{\rm B}$ = 3.5 V and $I_{\rm T}$ = 10 pA. The inset shows a close-up image of the newly converted 1T hexagonal phase ($V_B = -0.3 \text{ V}$; $I_T = 100 \text{ pA}$). (d) Histogram showing the number of islands converted from the stripe phase to the hexagonal phase and the minimum voltage pulse required for each conversion. Islands that did not exhibit a phase change from the stripe phase to the hexagonal phase for pulses of ≤5 V are counted as "nonconvertible" (NC).

Figure 2d. Stripe phase islands that did not convert into the hexagonal phase after the application of voltage pulses up to 5 V are denoted "nonconvertible" (NC). The phase conversion process is observed to be dependent on polarity, as no islands could be converted with negative pulses up to a magnitude of -4 V. At 5 K, 98% of all monolayer islands in the stripe phase could be converted to the hexagonal phase using positive pulses (Figure 2d) with an average threshold voltage $\langle V_{th} \rangle = 3.3$ V. No clear trend is seen regarding the area of the converted FeSe₂ region and the magnitude of the applied voltage pulse (see Figure S2). Possible mechanisms that might explain the 1T' to 1T phase transition observed here include the effect of the tip-induced electric field on local electronic dipole moments, ^{21,29} as well as the effect of electronic doping on the total energy of the two-dimensional film. ^{15,20}

The ease with which the stripe to hexagonal phase transition of FeSe₂ monolayers can be induced suggests a relatively low energy barrier between the stripe and hexagonal polymorphs. This implies that thermally induced island structural transitions

might be able to compete with tip-induced transitions at higher temperatures. To test this hypothesis and gain insight into the magnitude of the relevant energy barrier, we performed additional experiments at higher temperatures using the switching protocol described above. Figure 3a shows the tipinduced switching histogram for an ensemble of islands held at 20 K. The observed switching characteristics are very similar to those occurring at 5 K: all 23 islands were switched with $\langle V_{th} \rangle$ of 3.1 V. At higher temperatures, however, the switching behavior of the islands gradually changes. For example, Figure 3b shows that at 40 K the threshold voltage increases to 3.5 V and 11% of the islands are nonconvertible. At 50 K, the threshold voltage increases to 3.9 V and 27% of the islands cannot switch (Figure 3c). At 60 K, the threshold voltage increases further to $\langle V_{\rm th} \rangle$ of 4.4 V, while the nonswitching fraction increases to 54% (Figure 3d). The temperatureinduced trend is seen in Figure 3e, which shows the nonswitching fraction of islands as a function of temperature.

In addition to the apparent increased difficulty of switching with an increased temperature, we also observe islands switching back to the stripe phase at higher temperatures. For example, at 20 K no islands return to the stripe phase for waiting times on the order of 1 minute, while at 50 K, we observe 25% of the islands switching back to the stripe phase after a 1 minute waiting period. The increased difficulty of the 1T' to 1T phase transition with an increased temperature is likely influenced by the increased rate of back conversions. This is consistent with the fact that the striped 1T' phase of monolayer FeSe₂ is the thermodynamically stable phase.

The temperature dependence of the switching behavior can be visualized for a single monolayer island as shown in Figure 3f-i. Figure 3f shows the entire island in the stripe phase at 50 K before switching [the dashed black line shows a grain boundary between two rotated 1T' domains (see section 3 of the Supporting Information for additional discussion of domain boundaries). Figure 3g shows the island after being pulsed at the marked location, causing the lower right quadrant to switch to the hexagonal phase (50 K). The sample was then warmed up to 60 K over a period (Δt) of ~ 1 h, whereupon the same island was reimaged. As shown in Figure 3h, heating causes the island to switch back to the stripe phase with a grain boundary bisecting the island between two rotated 1T' domains (similar phase reversal also occurs for fully converted 1T islands as shown in section 4 of the Supporting Information). This island could not be switched to the hexagonal phase via tip pulsing at 60 K, but the 1T'-1T' rotational grain boundary did shift as a result of pulsing (Figure 3i) (similar tip pulse-induced movement of 1T'-1T' grain boundaries has been seen in TMDC monolayers previously²⁶).

To gain further insight into the properties of monolayer $FeSe_2$, we performed density functional theory (DFT) calculations using the DFT+U method with U values ranging from 0 to 6 eV for the Fe d orbital. As shown in Figure 4a, our relaxed DFT structures systematically underestimate the lattice constants of the 1T' and 1T $FeSe_2$ polymorphs by ~9% compared to the STM data (the energetically unfavorable 1H polymorph has a lattice constant that is >18% smaller than the experimental hexagonal lattice constant). Slight underestimation of lattice constants is common for DFT-based methods. Our DFT calculations provide useful insight into the energetics of the different $FeSe_2$ polymorphs, including their magnetic configurations. As shown in Figure 4b, the 1T'-FeSe $_2$ monolayer is the energetically favorable

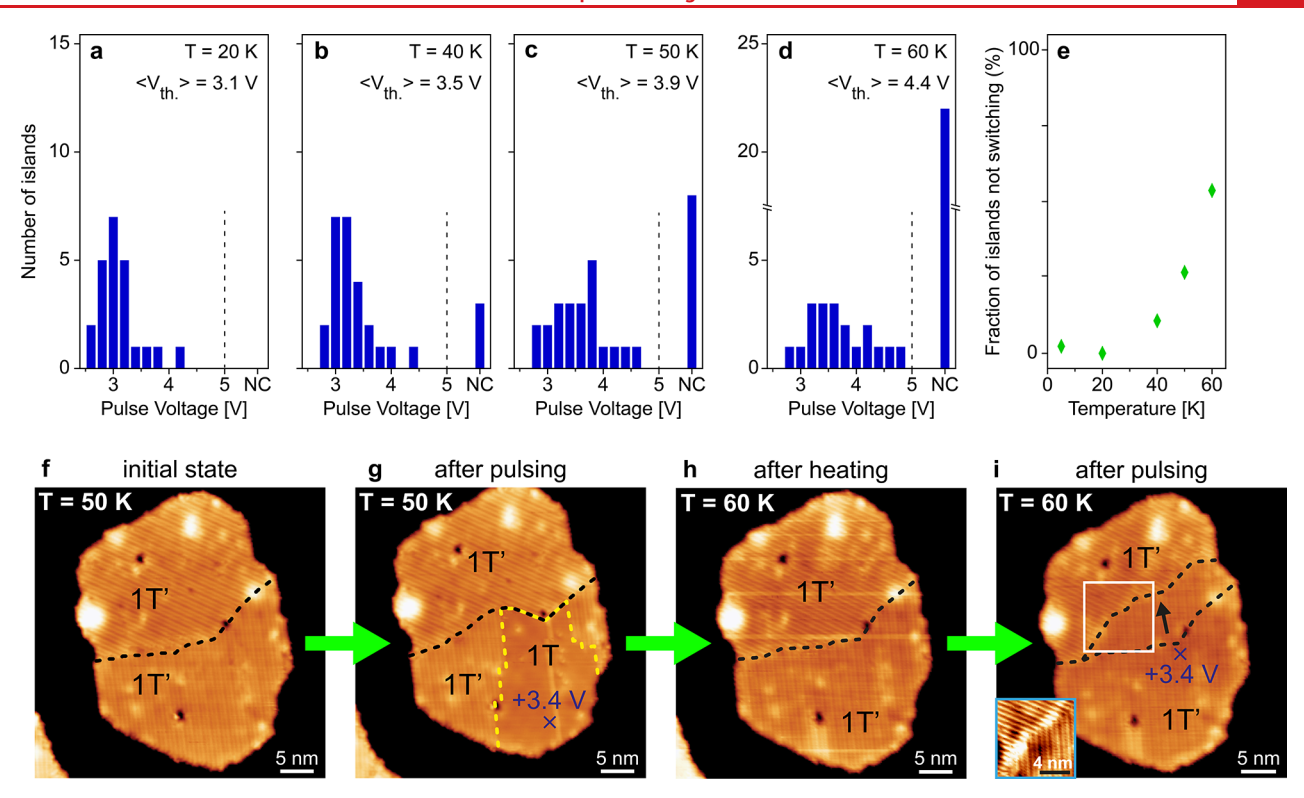


Figure 3. Thermal reversibility of the structural phase transition in FeSe₂ monolayers. Histograms show the number of monolayer islands converted from the stripe phase to the hexagonal phase (i.e., 1T' to 1T phase) and minimum voltage pulse required for conversion at (a) 20 K, (b) 40 K, (c) 50 K, and (d) 60 K. Islands not undergoing phase conversion for pulses of ≤ 5 V are counted as nonconvertible (NC). (e) Temperature dependence of the total fraction of islands counted as nonconvertible. STM images of the same monolayer FeSe₂ island (f) before and (g) after a 3.4 V pulse at the position indicated by the blue x. (h) Same island after the sample temperature is increased to 60 K. (i) Same island after the application of a 3.4 V pulse at the position depicted by the blue x (60 K). The boundary between two rotated stripe domains shifts after the voltage pulse as shown by the dashed black lines.

polymorph for U values of ≤ 4 eV [>160 meV/formula unit (f.u.) lower in energy than 1H-FeSe₂] but is only ~ 5 meV/f.u. more stable than monolayer 1T-FeSe₂ for U=4 eV. This leads to an energy difference of ~ 50 K between the 1T-FeSe₂ and 1T'-FeSe₂ phases, in reasonable agreement with the experimental results and supporting our choice of U=4 eV.

Our DFT calculations provide insight into the magnetic ground states of the different polymorphs of monolayer FeSe₂. Figure 4c shows that the 1T' rectangular AFM phase has the lowest energy of all of the polymorph phases, while the 1T FM phase is the nearest adjacent phase with an energy just 5 meV/f.u. higher (theoretically predicted magnetic orderings were seen to remain constant for electron and hole doping levels of $\leq 10^{13}~{\rm cm}^{-2}$). No experimental signatures of inelastically induced transitions between different theoretically predicted magnetic phases were observed for our FeSe₂ samples.

The magnetic moments of the 1T' rectangular AFM phase are predicted to have a magnitude of 3.59 $\mu_{\rm B}$ per Fe atom and 0.09 $\mu_{\rm B}$ per Se atom. The nearby 1T FM phase is predicted to have magnetic moments of 3.69 $\mu_{\rm B}$ per Fe atom and 0.12 $\mu_{\rm B}$ per Se atom (spin-polarized band structures for these magnetic configurations can be seen in Figure 4e and are compared to experimental dI/dV spectra in Figure S6). The ferromagnetic 1T-FeSe₂ monolayer adopts an in-plane magnetic configuration with a magnetic anisotropy barrier of 1.1 meV/f.u. (Figure 4d), consistent with an observed phase transition in magnetoresistance measured previously for multilayer 1T-FeSe₂ nanocrystals.³⁴

The calculated magnetic states of both 1T-FeSe_2 and 1T'-FeSe_2 are consistent with each Fe atom transferring four electrons to surrounding Se atoms, thus changing the Fe electron shell structure from $4\text{s}^23\text{d}^6$ to $4\text{s}^03\text{d}^4$. The four remaining d electrons are expected to result in 4 μ_B per Fe atom according to Hund's rule, which is reasonably consistent with our calculated magnetic moments. Because the Fe atoms in FeSe₂ are the next-nearest neighbors, the magnetic exchange interaction is likely dominated by superexchange coupling through Se atoms, whose sign and magnitude can strongly depend on bond lengths and bond angles. This is the probable cause of the different magnetic ground states between monolayer 1T-FeSe_2 and monolayer 1T'-FeSe_2 .

In conclusion, we have experimentally demonstrated the growth of the 1T' polymorph of monolayer FeSe₂, as well as reversible manipulation between monolayer FeSe₂ 1T' and 1T polymorphs. The 1T'-FeSe₂ to 1T-FeSe₂ transition is realized electrically upon application of a voltage pulse with the STM tip, while the 1T-FeSe₂ to 1T'-FeSe₂ transition is induced thermally. DFT simulations suggest that this structural phase transition is accompanied by a change from antiferromagnetic ordering in monolayer 1T'-FeSe₂ to ferromagnetic ordering in monolayer 1T-FeSe₂. The predicted difference in magnetic ordering between the 1T and 1T' phases combined with the experimentally observed reversible structural phase transition suggests that the magnetic ground state of FeSe₂ monolayers may be locally manipulated through their structural polymorph. FeSe₂ monolayers thus potentially provide a new

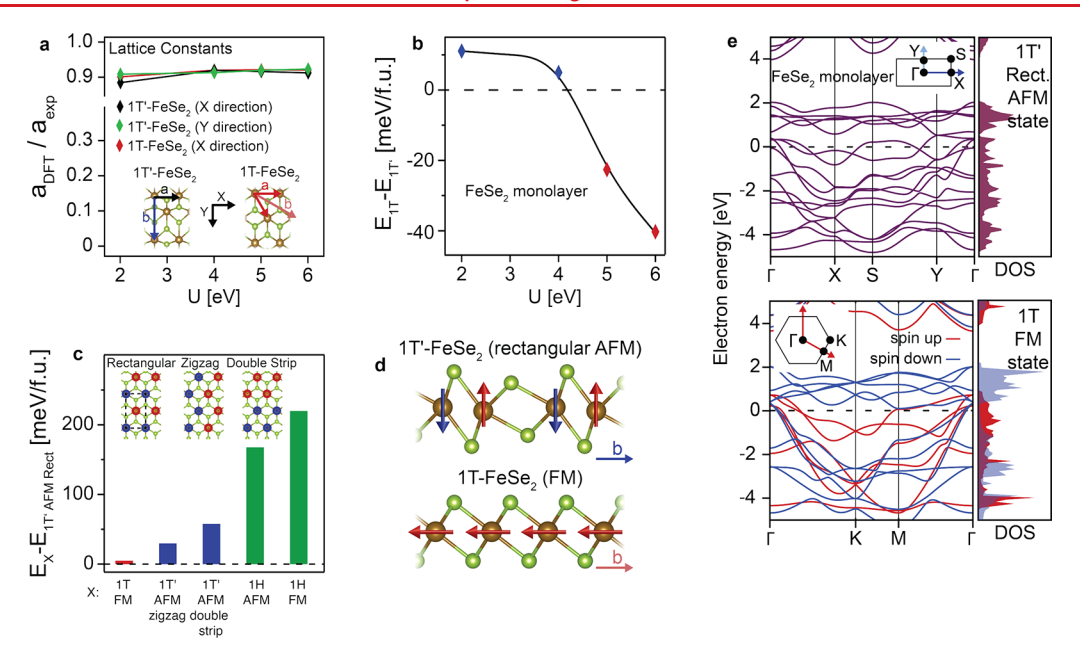


Figure 4. Calculated energetics of FeSe₂ monolayers. (a) Lattice constants of monolayer 1T'-FeSe₂ along the X direction (green), and monolayer 1T-FeSe₂ along the X direction (red) derived from DFT+U calculations for different values of U (normalized to the corresponding experimental lattice constants). (b) Total energy difference between the monolayer 1T- and 1T'-FeSe₂ structures as a function of Hubbard parameter U in DFT+U calculations. (c) Total energy difference between monolayer 1T'-FeSe₂ with a rectangular antiferromagnetic (AFM) configuration and different X-FeSe₂ polymorphs where $X = \{1T', 1T, 1H\}$ exhibiting different magnetic ground states (U = 4 eV). The inset shows the three possible calculated 1T' AFM configurations (red means spin up, and blue means spin down). (d) Magnetic ordering for monolayer 1T'-FeSe₂ in the rectangular AFM state and monolayer 1T-FeSe₂ in the FM state along the D direction as defined in panel (a) (the distorted D structure is exaggerated for the sake of clarity). (e) Band structure and density of states for rectangular AFM monolayer D and FM monolayer D and FM monolayer D states for rectangular AFM monolayer D and FM monolayer D and FM monolayer D states for rectangular AFM monolayer D and FM monolayer D and FM monolayer D states for rectangular AFM monolayer D and FM monolayer D states for rectangular AFM monolayer D states for rectangular AFM monolayer D and FM monolayer D states for rectangular AFM monolayer D states D states for rectangular AFM monolayer D states D states

platform for the investigation and manipulation of structural and magnetic phase transitions in the atomically thin limit.

■ METHODS

MBE Growth. Monolayer $FeSe_2$ samples were grown on highly oriented pyrolytic graphite (HOPG) or on bilayer graphene on SiC(0001) substrates using MBE. Before growth, the substrates were cleaned by annealing them at 900 K overnight under ultra-high-vacuum conditions with a pressure better than 2×10^{-10} mbar. Iron (purity of 99.995%, SPIE) and selenium (purity of 99.999%, Alfa Aesar) were then sublimated from an e-beam evaporator (flux of 0.08 Å/min) and a home-built Knudsen cell (flux of 8 Å/min), respectively, until the desired surface coverage was achieved while the sample was held at 800 K.

STM Measurements. The clean transfer of the sample from the MBE chamber to the STM chamber was achieved by capping the sample with 20 nm of amorphous Se to prevent degradation in air. Before STM measurement, the samples were annealed in UHV at $\sim\!200$ °C for 1 h to remove the Se capping layer and then transferred *in situ* to the low-temperature (5 K) STM stage. Some samples were directly transferred from the MBE chamber to the STM chamber through a UHV suitcase to confirm the quality of the Secapped samples.

STM measurements were performed in a low-temperature CreaTec UHV STM instrument operated at a pressure of $<2 \times 10^{-10}$ mbar (5 K for all STM measurements except where otherwise specified). Electrochemically etched tungsten tips were calibrated on a Cu(111) surface before performing other STM measurements. STS measurements were performed using standard lock-in techniques (frequency of 401 Hz). The STM

tip was grounded during these measurements, and bias voltages refer to the sample voltage.

To determine the lattice constants of epitaxial FeSe $_2$ monolayers, we first calibrated our STM instrument by obtaining atomic resolution of the underlying HOPG or graphene substrate. The STM set point before the application of voltage pulses for monolayer phase switching was typically $V_{\rm B}=-1~{\rm V}$ and $I_{\rm T}=10~{\rm pA}$. Voltage pulses of 2 V were first applied and then increased by 0.1 V until the stripe to hexagonal phase transition was observed via STM topography scans.

Computational Methods. Electronic structure calculations were performed using DFT as implemented in the VASP package. TAW pseudopotentials were used to describe the ionic potential of all atoms. We employed exchange-correlation functionals with self-consistent van der Waals corrections using the optPBE-vdW functional. $^{38-40}$ A $_{30} \times 15 \times 1$ k-point grid and a cutoff energy of 500 eV were employed. Energy and force convergence criteria were set to $_{30}^{-10}$ eV and $_{30}^{-10}$ eV/Å, respectively. The out-of-plane lattice vector was set to 30 Å. A $_{30}^{-10}$ U parameter was added to constrain the spatial extent of the Fe d orbitals, which are often too extended in standard DFT. This approach also helps to provide more accurate magnetic exchange couplings. We applied DFT+ $_{30}^{-10}$ corrections $_{30}^{-10}$ using the method of Dudarev et al.

ASSOCIATED CONTENT

Solution Supporting Information

The Supporting Information is available free of charge at https://pubs.acs.org/doi/10.1021/acs.nanolett.4c01286.

Atomic structure of the monolayer FeSe₂ stripe phase (section 1), statistics for the converted area versus

magnitude of voltage pulses (section 2), additional experimental data on domain walls (section 3), phase reversal for a fully converted 1T island (section 4), and experimental dI/dV spectra and calculated density of states (section 5) (PDF)

AUTHOR INFORMATION

Corresponding Authors

Michael F. Crommie — Department of Physics, University of California, Berkeley, California 94720, United States; Materials Sciences Division, Lawrence Berkeley National Laboratory, Berkeley, California 94720, United States; Kavli Energy NanoScience Institute at the University of California, Berkeley, and Lawrence Berkeley National Laboratory, Berkeley, California 94720, United States; orcid.org/0000-0001-8246-3444; Email: crommie@berkeley.edu

Tiancong Zhu — Department of Physics and Astronomy and Birck Nanotechnology Center, Purdue University, West Lafayette, Indiana 47907, United States; ⊚ orcid.org/0000-0003-2703-5652; Email: zhu1242@purdue.edu

Authors

Zehao He — Department of Physics and Department of Material Science and Engineering, University of California, Berkeley, California 94720, United States; Materials Sciences Division, Lawrence Berkeley National Laboratory, Berkeley, California 94720, United States; orcid.org/0000-0002-7761-679X

Shiva Prasad Poudel – Department of Physics and MonArk NSF Quantum Foundry, University of Arkansas, Fayetteville, Arkansas 72701, United States

Samuel Stolz – Department of Physics, University of California, Berkeley, California 94720, United States

Tianye Wang — Department of Physics, University of California, Berkeley, California 94720, United States; Materials Sciences Division, Lawrence Berkeley National Laboratory, Berkeley, California 94720, United States; orcid.org/0000-0002-8863-8054

Antonio Rossi — The Molecular Foundry, Lawrence Berkeley National Laboratory, Berkeley, California 94720, United States; © orcid.org/0000-0003-4574-7215

Feng Wang — Department of Physics, University of California, Berkeley, California 94720, United States; Materials Sciences Division, Lawrence Berkeley National Laboratory, Berkeley, California 94720, United States; Kavli Energy NanoScience Institute at the University of California, Berkeley, and Lawrence Berkeley National Laboratory, Berkeley, California 94720, United States

Sung-Kwan Mo – Advanced Light Source, Lawrence Berkeley National Laboratory, Berkeley, California 94720, United States; occid.org/0000-0003-0711-8514

Alexander Weber-Bargioni — The Molecular Foundry, Lawrence Berkeley National Laboratory, Berkeley, California 94720, United States

Zi Qiang Qiu — Department of Physics, University of California, Berkeley, California 94720, United States; Materials Sciences Division, Lawrence Berkeley National Laboratory, Berkeley, California 94720, United States; orcid.org/0000-0003-0680-0714

Salvador Barraza-Lopez — Department of Physics and MonArk NSF Quantum Foundry, University of Arkansas, Fayetteville, Arkansas 72701, United States; ⊙ orcid.org/0000-0002-4301-3317

Complete contact information is available at: https://pubs.acs.org/10.1021/acs.nanolett.4c01286

Author Contributions

[∇]Z.H., S.P.P., and S.S. contributed equally to this work.

The authors declare no competing financial interest.

ACKNOWLEDGMENTS

This research was supported by the Director, Office of Science, Office of Basic Energy Sciences, Materials Sciences and Engineering Division of the U.S. Department of Energy, under Contract DE-AC02-05CH11231 within the van der Waals heterostructures program (KCWF16) (STM and STS measurements). Support was also provided by the Center for Novel Pathways to Quantum Coherence in Materials, an Energy Frontier Research Center funded by the U.S. Department of Energy, Office of Science, Basic Energy Sciences (MBE film growth and characterization), Future Materials Discovery Program through the National Research Foundation of Korea (No. 2015M3D1A1070467) (substrate preparation and vacuum system development), and the National Science Foundation (NSF) under Grant DMR-2221750 (phase switching analysis). S.S. acknowledges fellowship support by the Swiss National Science Foundation under Project 195133. S.P.P. and S.B.L. were supported by the National Science Foundation Q-AMASE-i program under Grant DMR-1906383 (magnetic structure simulations). DFT calculations were performed at the University of Arkansas Pinnacle Supercomputer, funded by the NSF under Grant OAC-2346752.

■ REFERENCES

- (1) Manzeli, S.; Ovchinnikov, D.; Pasquier, D.; Yazyev, O. V.; Kis, A. 2D Transition Metal Dichalcogenides. *Nat. Rev. Mater.* **2017**, 2 (8), 1–15
- (2) Fei, Z.; Palomaki, T.; Wu, S.; Zhao, W.; Cai, X.; Sun, B.; Nguyen, P.; Finney, J.; Xu, X.; Cobden, D. H. Edge Conduction in Monolayer WTe₂. *Nat. Phys.* **2017**, *13* (7), 677–682.
- (3) Wu, S.; Fatemi, V.; Gibson, Q. D.; Watanabe, K.; Taniguchi, T.; Cava, R. J.; Jarillo-Herrero, P. Observation of the Quantum Spin Hall Effect up to 100 K in a Monolayer Crystal. *Science* **2018**, 359 (6371), 76–79.
- (4) Tang, S.; Zhang, C.; Wong, D.; Pedramrazi, Z.; Tsai, H.-Z.; Jia, C.; Moritz, B.; Claassen, M.; Ryu, H.; Kahn, S.; Jiang, J.; Yan, H.; Hashimoto, M.; Lu, D.; Moore, R. G.; Hwang, C.-C.; Hwang, C.; Hussain, Z.; Chen, Y.; Ugeda, M. M.; Liu, Z.; Xie, X.; Devereaux, T. P.; Crommie, M. F.; Mo, S.-K.; Shen, Z.-X. Quantum Spin Hall State in Monolayer 1T'-WTe₂. *Nat. Phys.* **2017**, *13* (7), 683–687.
- (5) Ugeda, M. M.; Bradley, A. J.; Zhang, Y.; Onishi, S.; Chen, Y.; Ruan, W.; Ojeda-Aristizabal, C.; Ryu, H.; Edmonds, M. T.; Tsai, H.-Z.; Riss, A.; Mo, S.-K.; Lee, D.; Zettl, A.; Hussain, Z.; Shen, Z.-X.; Crommie, M. F. Characterization of Collective Ground States in Single-Layer NbSe₂. *Nat. Phys.* **2016**, *12* (1), 92–97.
- (6) Vano, V.; Amini, M.; Ganguli, S. C.; Chen, G.; Lado, J. L.; Kezilebieke, S.; Liljeroth, P. Artificial Heavy Fermions in a van Der Waals Heterostructure. *Nature* **2021**, *599* (7886), *582*–*586*.
- (7) Chen, P.; Chan, Y.-H.; Fang, X.-Y.; Zhang, Y.; Chou, M. Y.; Mo, S.-K.; Hussain, Z.; Fedorov, A.-V.; Chiang, T.-C. Charge Density Wave Transition in Single-Layer Titanium Diselenide. *Nat. Commun.* **2015**, *6* (1), 8943.
- (8) Feng, J.; Biswas, D.; Rajan, A.; Watson, M. D.; Mazzola, F.; Clark, O. J.; Underwood, K.; Marković, I.; McLaren, M.; Hunter, A.; Burn, D. M.; Duffy, L. B.; Barua, S.; Balakrishnan, G.; Bertran, F.; Le Fèvre, P.; Kim, T. K.; van der Laan, G.; Hesjedal, T.; Wahl, P.; King,

- P. D. C. Electronic Structure and Enhanced Charge-Density Wave Order of Monolayer VSe₂. Nano Lett. **2018**, 18 (7), 4493–4499.
- (9) Duvjir, G.; Choi, B. K.; Jang, I.; Ulstrup, S.; Kang, S.; Thi Ly, T.; Kim, S.; Choi, Y. H.; Jozwiak, C.; Bostwick, A.; Rotenberg, E.; Park, J.-G.; Sankar, R.; Kim, K.-S.; Kim, J.; Chang, Y. J. Emergence of a Metal—Insulator Transition and High-Temperature Charge-Density Waves in VSe₂ at the Monolayer Limit. *Nano Lett.* **2018**, *18* (9), 5432–5438.
- (10) O'Hara, D. J.; Zhu, T.; Trout, A. H.; Ahmed, A. S.; Luo, Y. K.; Lee, C. H.; Brenner, M. R.; Rajan, S.; Gupta, J. A.; McComb, D. W.; Kawakami, R. K. Room Temperature Intrinsic Ferromagnetism in Epitaxial Manganese Selenide Films in the Monolayer Limit. *Nano Lett.* **2018**, *18* (5), 3125–3131.
- (11) Zhang, X.; Lu, Q.; Liu, W.; Niu, W.; Sun, J.; Cook, J.; Vaninger, M.; Miceli, P. F.; Singh, D. J.; Lian, S.-W.; Chang, T.-R.; He, X.; Du, J.; He, L.; Zhang, R.; Bian, G.; Xu, Y. Room-Temperature Intrinsic Ferromagnetism in Epitaxial CrTe₂ Ultrathin Films. *Nat. Commun.* **2021**, *12* (1), 2492.
- (12) Nakata, Y.; Sugawara, K.; Shimizu, R.; Okada, Y.; Han, P.; Hitosugi, T.; Ueno, K.; Sato, T.; Takahashi, T. Monolayer 1T-NbSe₂ as a Mott Insulator. *NPG Asia Mater.* **2016**, 8 (11), e321–e321.
- (13) Chen, Y.; Ruan, W.; Wu, M.; Tang, S.; Ryu, H.; Tsai, H.-Z.; Lee, R.; Kahn, S.; Liou, F.; Jia, C.; Albertini, O. R.; Xiong, H.; Jia, T.; Liu, Z.; Sobota, J. A.; Liu, A. Y.; Moore, J. E.; Shen, Z.-X.; Louie, S. G.; Mo, S.-K.; Crommie, M. F. Strong Correlations and Orbital Texture in Single-Layer 1T-TaSe₂. *Nat. Phys.* **2020**, *16*, 218–224.
- (14) Song, S.; Keum, D. H.; Cho, S.; Perello, D.; Kim, Y.; Lee, Y. H. Room Temperature Semiconductor–Metal Transition of MoTe₂ Thin Films Engineered by Strain. *Nano Lett.* **2016**, *16* (1), 188–193.
- (15) Wang, Y.; Xiao, J.; Zhu, H.; Li, Y.; Alsaid, Y.; Fong, K. Y.; Zhou, Y.; Wang, S.; Shi, W.; Wang, Y.; Zettl, A.; Reed, E. J.; Zhang, X. Structural Phase Transition in Monolayer MoTe₂ Driven by Electrostatic Doping. *Nature* **2017**, 550 (7677), 487–491.
- (16) Zhu, X.; Li, D.; Liang, X.; Lu, W. D. Ionic Modulation and Ionic Coupling Effects in MoS₂ Devices for Neuromorphic Computing. *Nat. Mater.* **2019**, *18* (2), 141–148.
- (17) Maximenko, Y.; Chang, Y.; Chen, G.; Hirsbrunner, M. R.; Swiech, W.; Hughes, T. L.; Wagner, L. K.; Madhavan, V. Nanoscale Studies of Electric Field Effects on Monolayer 1T'-WTe₂. *Npj Quantum Mater.* **2022**, *7* (1), 1–6.
- (18) Zhu, T.; Ruan, W.; Wang, Y.-Q.; Tsai, H.-Z.; Wang, S.; Zhang, C.; Wang, T.; Liou, F.; Watanabe, K.; Taniguchi, T.; Neaton, J. B.; Weber-Bargioni, A.; Zettl, A.; Qiu, Z. Q.; Zhang, G.; Wang, F.; Moore, J. E.; Crommie, M. F. Imaging Gate-Tunable Tomonaga—Luttinger Liquids in 1H-MoSe₂ Mirror Twin Boundaries. *Nat. Mater.* 2022, 21 (7), 748–753.
- (19) Duerloo, K.-A. N.; Li, Y.; Reed, E. J. Structural Phase Transitions in Two-Dimensional Mo- and W-Dichalcogenide Monolayers. *Nat. Commun.* **2014**, *5* (1), 4214.
- (20) Li, Y.; Duerloo, K.-A. N.; Wauson, K.; Reed, E. J. Structural Semiconductor-to-Semimetal Phase Transition in Two-Dimensional Materials Induced by Electrostatic Gating. *Nat. Commun.* **2016**, *7* (1), 10671.
- (21) Zhang, J.; Liu, J.; Huang, J. L.; Kim, P.; Lieber, C. M. Creation of Nanocrystals Through a Solid-Solid Phase Transition Induced by an STM Tip. *Science* **1996**, 274 (5288), 757–760.
- (22) Kim, J.-J.; Park, C.; Yamaguchi, W.; Shiino, O.; Kitazawa, K.; Hasegawa, T. Observation of a Phase Transition from the T Phase to the H Phase Induced by a STM Tip in 1T-TaS₂. *Phys. Rev. B* **1997**, *56* (24), R15573–R15576.
- (23) Bischoff, F.; Auwärter, W.; Barth, J. V.; Schiffrin, A.; Fuhrer, M.; Weber, B. Nanoscale Phase Engineering of Niobium Diselenide. *Chem. Mater.* **2017**, *29* (23), 9907–9914.
- (24) Zhang, F.; Wang, Z.; Dong, J.; Nie, A.; Xiang, J.; Zhu, W.; Liu, Z.; Tao, C. Atomic-Scale Observation of Reversible Thermally Driven Phase Transformation in 2D In₂Se₃. ACS Nano **2019**, 13 (7), 8004–8011.
- (25) Cho, S.; Kim, S.; Kim, J. H.; Zhao, J.; Seok, J.; Keum, D. H.; Baik, J.; Choe, D.-H.; Chang, K. J.; Suenaga, K.; Kim, S. W.; Lee, Y.

- H.; Yang, H. Phase Patterning for Ohmic Homojunction Contact in MoTe₂. Science **2015**, 349 (6248), 625–628.
- (26) Pedramrazi, Z.; Herbig, C.; Pulkin, A.; Tang, S.; Phillips, M.; Wong, D.; Ryu, H.; Pizzochero, M.; Chen, Y.; Wang, F.; Mele, E. J.; Shen, Z.-X.; Mo, S.-K.; Yazyev, O. V.; Crommie, M. F. Manipulating Topological Domain Boundaries in the Single-Layer Quantum Spin Hall Insulator 1T'–WSe₂. *Nano Lett.* **2019**, *19*, 5634–5639.
- (27) Song, C.-L.; Wang, Y.-L.; Jiang, Y.-P.; Li, Z.; Wang, L.; He, K.; Chen, X.; Ma, X.-C.; Xue, Q.-K. Molecular-Beam Epitaxy and Robust Superconductivity of Stoichiometric FeSe Crystalline Films on Bilayer Graphene. *Phys. Rev. B* **2011**, *84* (2), 020503.
- (28) Lee, J.; Wong, D.; Velasco Jr, J.; Rodriguez-Nieva, J. F.; Kahn, S.; Tsai, H.-Z.; Taniguchi, T.; Watanabe, K.; Zettl, A.; Wang, F.; Levitov, L. S.; Crommie, M. F. Imaging Electrostatically Confined Dirac Fermions in Graphene Quantum Dots. *Nat. Phys.* **2016**, *12* (11), 1032–1036.
- (29) Chang, K.; Küster, F.; Miller, B. J.; Ji, J.-R.; Zhang, J.-L.; Sessi, P.; Barraza-Lopez, S.; Parkin, S. S. P. Microscopic Manipulation of Ferroelectric Domains in SnSe Monolayers at Room Temperature. *Nano Lett.* **2020**, 20 (9), 6590–6597.
- (30) Perdew, J. P.; Ruzsinszky, A.; Csonka, G. I.; Vydrov, O. A.; Scuseria, G. E.; Constantin, L. A.; Zhou, X.; Burke, K. Restoring the Density-Gradient Expansion for Exchange in Solids and Surfaces. *Phys. Rev. Lett.* **2008**, *100* (13), 136406.
- (31) Winiarski, M. J.; Samsel-Czekała, M.; Ciechan, A. Strain Effects on the Electronic Structure of the Iron Selenide Superconductor. *EPL Europhys. Lett.* **2012**, *100* (4), 47005.
- (32) Zhang, G.-X.; Reilly, A. M.; Tkatchenko, A.; Scheffler, M. Performance of Various Density-Functional Approximations for Cohesive Properties of 64 Bulk Solids. *New J. Phys.* **2018**, 20 (6), 063020.
- (33) Li, T.; Zhang, X.; Zeng, Z. Factors Affecting the Electron—Phonon Coupling in FeSe under Pressure. *Phys. Chem. Chem. Phys.* **2021**, 23 (44), 25107–25113.
- (34) Liu, H.; Xue, Y. Van Der Waals Epitaxial Growth and Phase Transition of Layered FeSe₂ Nanocrystals. *Adv. Mater.* **2021**, 33 (17), 2008456.
- (35) Kresse, G.; Furthmüller, J. Efficient Iterative Schemes for Ab Initio Total-Energy Calculations Using a Plane-Wave Basis Set. *Phys. Rev. B* **1996**, *54* (16), 11169–11186.
- (36) Kresse, G.; Joubert, D. From Ultrasoft Pseudopotentials to the Projector Augmented-Wave Method. *Phys. Rev. B* **1999**, *59* (3), 1758–1775.
- (37) Berland, K.; Cooper, V. R.; Lee, K.; Schröder, E.; Thonhauser, T.; Hyldgaard, P.; Lundqvist, B. I. Van Der Waals Forces in Density Functional Theory: A Review of the vdW-DF Method. *Rep. Prog. Phys.* **2015**, 78 (6), 066501.
- (38) Klimeš, J.; Bowler, D. R.; Michaelides, A. Chemical Accuracy for the van Der Waals Density Functional. *J. Phys.: Condens. Matter* **2010**, 22 (2), 022201.
- (39) Lee, K.; Murray, É. D.; Kong, L.; Lundqvist, B. I.; Langreth, D. C. Higher-Accuracy van Der Waals Density Functional. *Phys. Rev. B* **2010**, 82 (8), 081101.
- (40) Klimeš, J.; Bowler, D. R.; Michaelides, A. Van Der Waals Density Functionals Applied to Solids. *Phys. Rev. B* **2011**, 83 (19), 195131.
- (41) Anisimov, V. I.; Gunnarsson, O. Density-Functional Calculation of Effective Coulomb Interactions in Metals. *Phys. Rev. B* **1991**, 43 (10), 7570–7574.
- (42) Anisimov, V. I.; Zaanen, J.; Andersen, O. K. Band Theory and Mott Insulators: Hubbard U Instead of Stoner I. *Phys. Rev. B* **1991**, *44* (3), 943–954.
- (43) Dudarev, S. L.; Botton, G. A.; Savrasov, S. Y.; Humphreys, C. J.; Sutton, A. P. Electron-Energy-Loss Spectra and the Structural Stability of Nickel Oxide: An LSDA+U Study. *Phys. Rev. B* **1998**, *57* (3), 1505–1509.